



Morphological Transition of the Compact Radio Lobe in 3C 84 via the Strong Jet–Cloud Collision

Motoki Kino^{1,2}, Kotaro Niinuma^{3,4}, Nozomu Kawakatu⁵, Hiroshi Nagai^{2,6}, Gabriele Giovannini^{7,8}, Monica Orienti⁷, Kiyooki Wajima^{9,10}, Filippo D’Ammando⁷, Kazuhiro Hada^{6,11}, Marcello Giroletti⁷, and Mark Gurwell¹²

¹ Kogakuin University of Technology & Engineering, Academic Support Center, 2665-1 Nakano, Hachioji, Tokyo 192-0015, Japan; motoki.kino@nao.ac.jp

² National Astronomical Observatory of Japan, 2-21-1 Osawa, Mitaka, Tokyo 181-8588, Japan

³ The Research Institute of Time Studies, Yamaguchi University, 1677-1 Yoshida, Yamaguchi-city, Yamaguchi 753-8511, Japan

⁴ Graduate School of Sciences and Technology for Innovation, Yamaguchi University, 1677-1 Yoshida, Yamaguchi, Yamaguchi 753-8512, Japan

⁵ National Institute of Technology, Kure College, 2-2-11, Agaminami, Kure, Hiroshima 737-8506, Japan

⁶ Department of Astronomical Science, The Graduate University for Advanced Studies, SOKENDAI, 2-21-1 Osawa, Mitaka, Tokyo 181-8588, Japan

⁷ INAF—Istituto di Radioastronomia, via Gobetti 101, I-40129 Bologna, Italy

⁸ Dipartimento di Fisica e Astronomia, Università di Bologna, via Gobetti 103/2, I-40129 Bologna, Italy

⁹ Korea Astronomy and Space Science Institute, 776 Daedeokdae-ro, Yuseong-gu, Daejeon 34055, Republic of Korea

¹⁰ Department of Astronomy and Space Science, University of Science and Technology, 217 Gajeong-ro, Yuseong-gu, Daejeon 34113, Republic of Korea

¹¹ Mizusawa VLBI Observatory, National Astronomical Observatory of Japan, 2-21-1 Osawa, Mitaka, Tokyo 181-8588, Japan

¹² Center for Astrophysics | Harvard & Smithsonian, 60 Garden Street, Cambridge, MA 02138, USA

Received 2021 August 10; revised 2021 September 4; accepted 2021 September 8; published 2021 October 11

Abstract

We report multiepoch very long baseline interferometric observations of the compact radio lobe in the radio galaxy 3C 84 (NGC 1275) during 2016–2020. The image sequence of 3C 84 reveals that the hotspot in the radio lobe showed the 1 year long frustration in 2017 within a compact region of about 0.07 pc, suggesting a strong collision between the jet and a compact dense cloud with an estimated average density of about $(4\text{--}6) \times 10^5 \text{ cm}^{-3}$. Although the hotspot and the radio lobe began to move south again after its breakout, the radio lobe showed a morphological transition from an FR II- to FR I-class radio lobe and its radio flux became fainter. This is the first detection of the dynamical feedback from the cloud to the jet where the cloud located on the jet axis significantly interferes with the jet propagation and evolution at the central 1 pc region in the active galactic nucleus.

Unified Astronomy Thesaurus concepts: Radio galaxies (1343); Active galactic nuclei (16); Radio continuum emission (1340)

1. Introduction

Radio jets in active galactic nuclei (AGNs) are considered to be one of the major drivers of galaxy evolution and understanding how jets carry energy from the central nucleus to large scales is one of the most fundamental questions (e.g., Fabian 2012; Kormendy & Ho 2013, for review). Radio lobes associated with the jets are key structures reflecting the history of the jet propagation and its radio-mode feedback to the surrounding matter (e.g., Croton et al. 2006; Wagner et al. 2012). The radio lobes are classified into two classes. While Fanaroff–Riley class I (FR I) are core-brightened with a fainter outer edge of the radio lobes, Fanaroff–Riley class II (FR II) are edge-brightened with bright hotspots at the ends of their lobes (Fanaroff & Riley 1974). There are two scenarios for the origin of the FR I/FR II divide. One is due to a different nature of the central engine that drives the jet (e.g., Rawlings & Saunders 1991; Baum et al. 1995; Meier et al. 1997; Ghisellini & Celotti 2001), while the other is due to a different degree of deceleration caused by intergalactic matter (e.g., Kawakatu et al. 2008; Kharb et al. 2012; Laing & Bridle 2014). The purpose of this study is to explore energy transport by radio lobes on parsec scales that has yet to be studied sufficiently.

The nearby radio galaxy 3C 84 ($z = 0.0176$) at the center of the Perseus cluster, harboring a supermassive black hole with a mass of $M_{\text{BH}} = (0.8\text{--}2) \times 10^9 M_{\odot}$ (Scharwachter et al. 2013; Giovannini et al. 2018) is an excellent laboratory for exploring the physics of energy transport by radio lobes at parsec scales. The C3 component in 3C 84 is known as a newborn radio-lobe component associated with the radio outburst that started in 2005 and it propagates southward and becomes brighter (Nagai et al. 2010;

Hiura et al. 2018). The brightness peak in the C3 component is identified as the hotspot, which is a termination shock at the tip of the jet. The peculiar structure of C3 suggests interactions between the jet and the surrounding medium (Giovannini et al. 2018) and a recent very long baseline interferometric (VLBI) observation found a positional flip of the hotspot in 2015 September that indicated the jet and cloud interaction (Kino et al. 2018). Very Long Baseline Array (VLBA) data also showed an enhancement of a linearly polarized flux that also supports the jet–cloud interaction (Nagai et al. 2017). In this Letter, we report continuous VLBI monitoring observations of 3C 84 that reveals further strong jet–cloud collision that accompanies morphological transition of the radio lobe. With the cosmology parameters of $\Omega_m = 0.27$, $\Omega_{\Lambda} = 0.73$, and $H_0 = 71 \text{ km s}^{-1} \text{ Mpc}^{-1}$ (Komatsu et al. 2009) the angular scale of 1 mas corresponds to a linear distance of 0.35 pc for 3C 84.

2. Observations and Data Reductions

We have conducted the high-cadence monitoring observations of 3C 84 with the Korean VLBI network and VERA Array (KaVA) array at 43 GHz during 2016–2018. Imaging capabilities of KaVA are summarized in Niinuma et al. (2014). The typical size of the original beam of KaVA at 43 GHz is 0.6–0.7 mas (see also Kino et al. 2018; Wajima et al. 2020). At 22 GHz, we have conducted another high-cadence monitoring observation with the VLBI Exploration of Radio Astronomy (VERA) array in the framework of the Gamma-ray Emitting Notable AGN Monitoring with Japanese VLBI (GENJI) program. Data reduction was performed using the National Radio Astronomy Observatory Astronomical Imaging Processing System in the same way

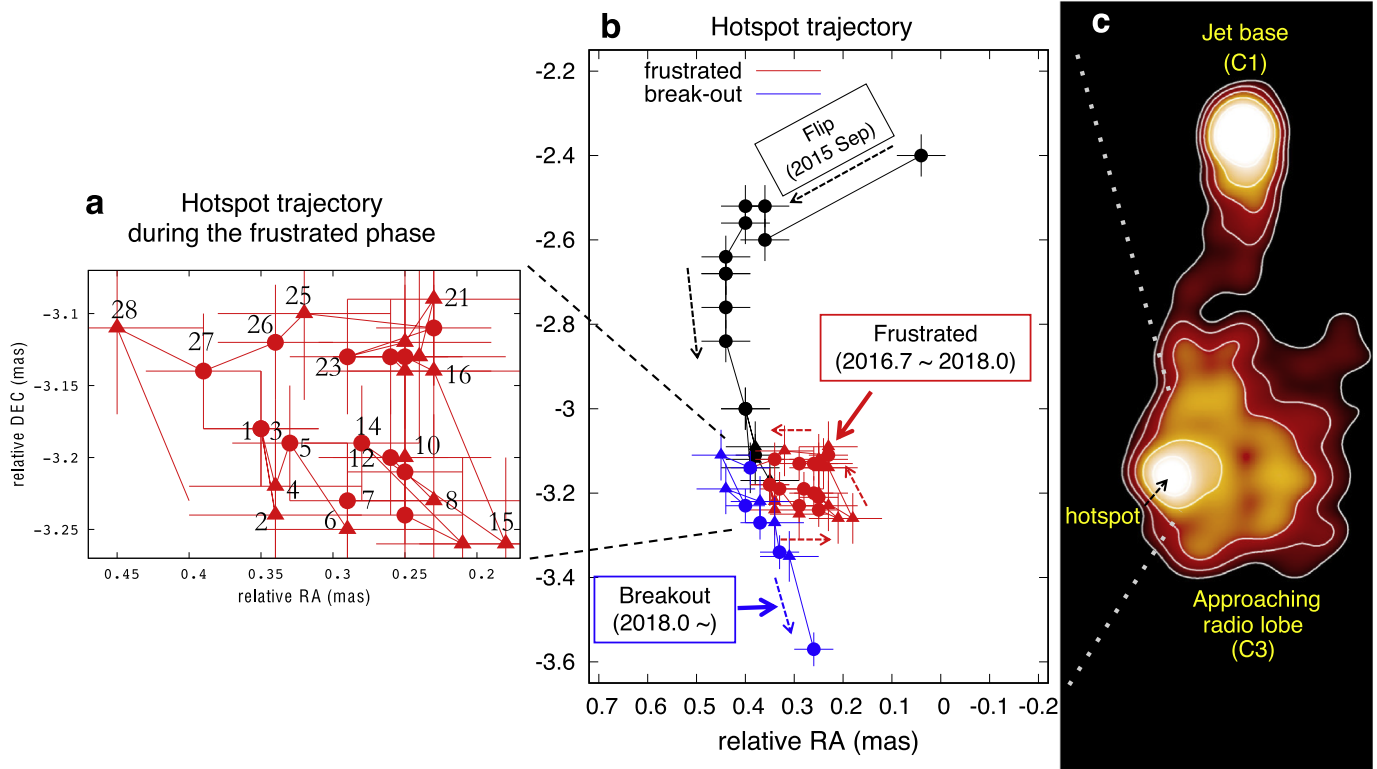


Figure 1. Trajectory of the hotspot in C3. (a) Zoomed-in view of the hotspot (the brightness peak position in C3) trajectory during the frustrated phase. The number next to each position data indicates the epoch number (28 epochs in total). During the frustrated phase, the positions of the hotspot were not random, but they showed a counterclockwise trajectory. The circle dots correspond to the data points measured by KaVA, while the triangle dots are those measured by VLBA. (b) Overall sequence of the brightness peak position change the hotspot component. The arrows indicate the time sequence of the position. The flip of the hotspot was found in 2015 September (Kino et al. 2018). As shown in panel (a), the position of the hotspot showed the counter-rotating trajectory in the sky plane in the compact region with its projected angular size of about 0.2 mas (red dots). After the frustrated phase, the C3 resumed to propagate moving south (blue points). (c) The entire image of the 3C 84 jet with VLBA at 43 GHz. The C1 component corresponds to the jet base containing the central engine that drives the jet.

described in the GENJI program (Nagai et al. 2013; Hiura et al. 2018). A priori amplitude calibration was applied using the measured system noise temperature and the elevation-gain curve of each antenna. We calibrated the bandpass characteristics of phase and amplitude at each station using the autocorrelation data. Following the amplitude calibration, fringe-fitting was performed to calibrate the visibility phases. Finally, the data were averaged over each intermediate frequency band. The imaging and self-calibration were performed in the Difmap software in the usual manner. We also included VLBA 43 GHz archived data obtained in the blazar monitoring program led by Boston University Group.¹³ To determine the brightness peak position of the C3 component, we performed a two-dimensional Gaussian fit to the visibility data by using the Difmap task modelfit. In the process, we trimmed off VLBA visibility data on the baselines longer than $350 M\lambda$ to align with KaVA’s uv -coverage. For better understanding of the light-curve behavior, we included the Submillimeter Array (SMA) monitoring data at 1.3 mm. Detailed explanations for the monitoring program are described in the literature (Gurwell et al. 2007).

3. Results

3.1. Discovery of the Frustrated Hotspot

In Figure 1, we present the time sequence of the positional change of the hotspot obtained from more than 50 epochs of

images observed with KaVA and VLBA at 43 GHz. One can readily see new important findings as follows: (1) As shown in the panel (b) of Figure 1, the position of the hotspot was frustrated during the period from 2016.7 to 2018.0. The location of the hotspot during the frustrated phase was confined within a compact region with its angular size about 0.2 mas, which is equivalent to about 0.07 pc in the projected physical scale. (2) The trajectory of the hotspot during the frustrated phase was not random but rather smoothly connected between neighboring epochs and it showed an apparent counterclockwise rotating motion on the sky plane (shown in the panel (a) of Figure 1). The trajectory of the hotspot may remind us of a similarity with the dentist-drill model proposed by Scheuer (1982) where hotspots show vivid wobbling. (3) After 2018.0, it broke out and began to move south again. This frustration and breakout of the hotspot cannot be explained by a global change of the entire jet direction due to the precession of the jet base (Hiura et al. 2018), while a strong collision between the jet and a compact dense cloud at this local site can naturally account for them.

In Figure 2, we summarize the overall picture of the hotspot trajectory relative to the peak position of the jet base (hereafter C1). The projected distance from the jet base (C1) to C3 was about a 1 pc scale during our observational period. One can see the overall trajectory of the hotspot toward the south. In the beginning, the abrupt large flip of the hotspot position was found in 2015 August–September and it was explained as an off-axis collision between the jet and a dense cloud (Kino et al. 2018). After the flip in 2015, the hotspot propagated toward

¹³ <https://www.bu.edu/blazars/>

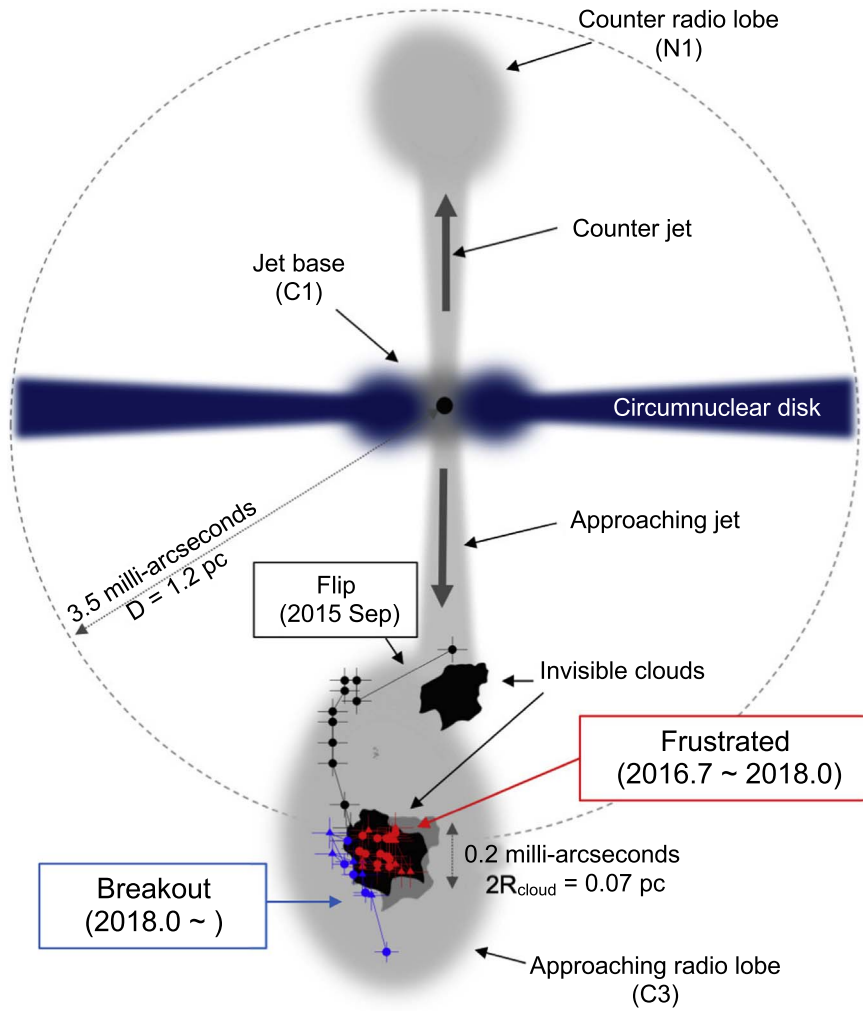


Figure 2. The observed trajectory of the hotspot overlaid onto a schematic picture of the central parsec-scale region of 3C 84. Before the frustrated phase (the black dots), the C3 component continued to propagate toward the south. In the period from late 2016 to the end of 2017, we discovered 1.3 yr of frustration of the hotspot in C3 (red dots). For completeness, we add an illustration of the counter lobe component (N1), whose radio emission is largely interrupted by free–free absorption caused by the foreground circumnuclear disk (Walker et al. 2000; Wajima et al. 2020).

south until the middle of 2016. Then, the hotspot suddenly stopped its propagation over the period from 2016.7 (fourth epoch in the red dot data) to 2018.0 (i.e., $t_{\text{frust}} \approx 1.3$ yr). Such a phenomenon has never been found in AGN jets. The strong head-on collision releases the bulk kinetic energy of the 3C 84 jet into other forms of energy. The amount of the released energy by the collision is one of the most interesting quantities, and it can be estimated as $E_{\text{feedback}} \approx L_{\text{jet}} t_{\text{frust}}$. Since the duration of the frustration and the size of the cloud are directly determined from the kinematics of the hotspot, we obtain $E_{\text{feedback}} \approx 4 \times 10^{52-53}$ erg where the value of the total jet kinetic power of 3C 84 is $L_{\text{jet}} \approx 1 \times 10^{45-46}$ erg s $^{-1}$ suggested by the dynamics of the X-ray cavity in the Perseus cluster inflated by the jet kinetic power (Heinz et al. 1998; Churazov et al. 2000). In Section 4, we will discuss possible usages of E_{feedback} .

3.2. Light Curves

In the left panel of Figure 3, we show the light curves of the C3 component during 2016–2018. As will be explained below, the light-curve data also agree well with the prediction of the

jet–cloud collision. The radio flux densities at 22, 43, and 230 GHz decreased during the frustrated phase (red dots). These decreases stopped when they entered the breakout phase (blue dots). The synchronization of the period of frustration with that of flux density decrease (red dots) among 22, 43, and 230 GHz suggests an absorption phenomenon. Since the hotspot is expected to be buried in the cloud during the collision, the radio emission from the hotspot is considered to be partially absorbed by the cloud. The faster decrease of the radio flux at 22 GHz than that of 43 GHz supports the free–free absorption (FFA) that is seen against the counter radio-lobe component (e.g., Fujita & Nagai 2017; Walker et al. 2000; Wajima et al. 2020; see N1 in Figure 2). Since the degree of FFA depends on the number density of the cloud (n_{cloud}), we can constrain n_{cloud} . In the past, the C3 component had an optically thin spectrum between 22–43 GHz ($\alpha_{22-43} < 0$), which showed $\alpha_{22-43} \sim -0.9$ in 2008 (e.g., Suzuki et al. 2012). During the frustrated phase, it increased and it maximally reached to $\alpha_{22-43} \sim 0.5$. Below, we constrain n_{cloud} based on this α_{22-43} value. It is known that the FFA opacity is given by $\tau_{\text{FFA}}(\nu) \approx 2.7 \left(\frac{T_{\text{cloud}}}{10^4 \text{ K}} \right)^{-3/2} \left(\frac{n_{\text{cloud}}}{10^5 \text{ cm}^{-3}} \right)^{-2} \left(\frac{l_{\text{cloud}}}{0.1 \text{ pc}} \right)^1 \left(\frac{\nu}{43 \text{ GHz}} \right)^{-2}$,

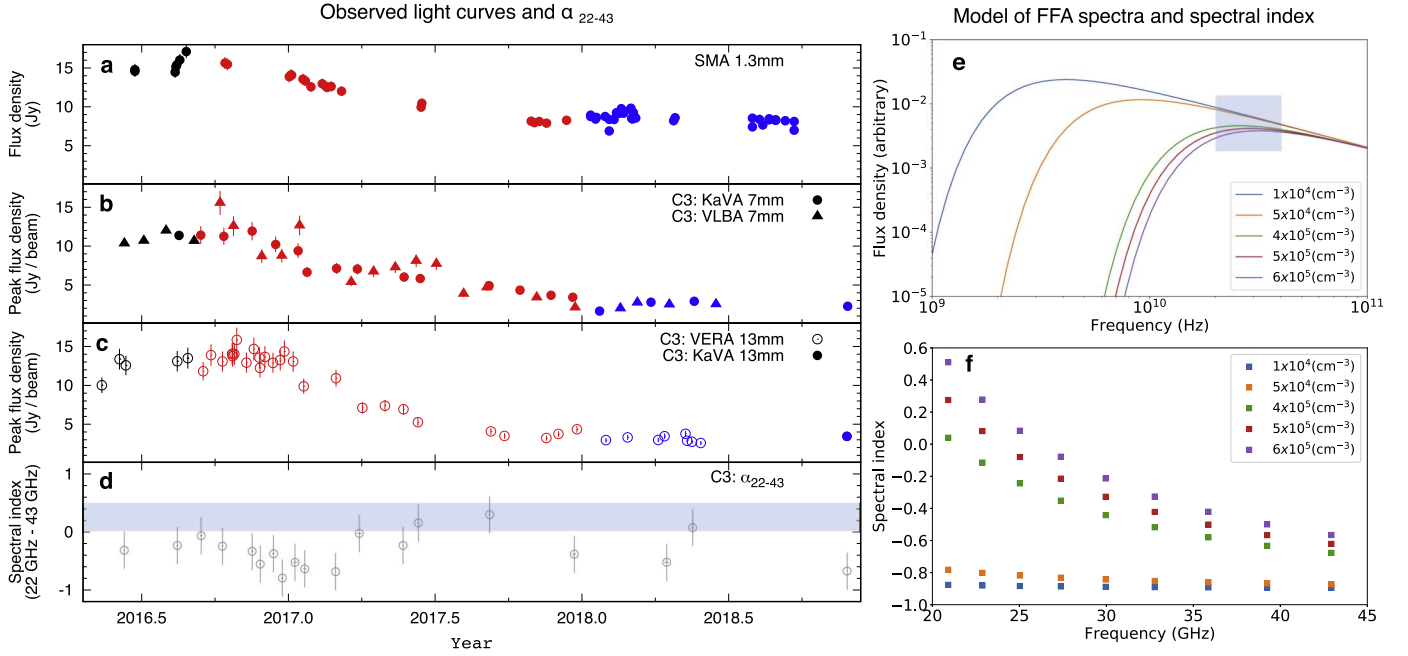


Figure 3. Left: observed light curves of the C3 component from 22 GHz (13 mm) to 230 GHz (1.3 mm). (a) The light curves of 3C 84 at 1.3 mm with SMA is presented. (b) The light curve of the C3 component observed at 7 mm with KaVA and VLBA is shown. (c) The light curve of the C3 component observed at 13 mm with VERA and KaVA is presented. Some error bars cannot be seen because they are smaller than each symbol. In panels (a)–(c), the black, red, and blue dots are the data for the period before, during, and after the frustrated phase (breakout), respectively. We show the peak flux densities at 22 GHz and 43 GHz convolved with 1.0 mas and 0.75 mas circular Gaussian beams, respectively. While it is clear that the flux significantly decreased during the frustrated period in all three frequency bands, it is also evident that the dimming stopped after the breakout. (d) Time variation of the spectral index of C3 between 22 and 43 GHz α_{22-43} . We derived α_{22-43} from the peak flux densities convolved with 1 mas at 22 and 43 GHz quasi-simultaneously acquired within a period of 3 days. Right: (e) the top right panel shows the n_{cloud} dependence of the model predicted synchrotron spectra in arbitrary unit. It can be seen that the spectrum on the low-frequency side is more strongly affected by FFA absorption as n_{cloud} increases. (f) The bottom right panel shows the corresponding n_{cloud} dependence of the spectral indices for each frequency. When the density increases to $n_{\text{cloud}} \approx (4-6) \times 10^5 \text{ cm}^{-3}$ the positive spectral index can be realized.

where T_{cloud} and l_{cloud} are the temperature and the path-length of the dense cloud, respectively (e.g., Levinson et al. 1995; Fujita & Nagai 2017). The observed synchrotron flux density becomes smaller than the intrinsic flux density by a factor of $\exp[-\tau_{\text{FFA}}(\nu)]$. In the right panel of Figure 3, we show the n_{cloud} dependence of the FFA synchrotron flux densities. To realize the inverted spectra with $0 \lesssim \alpha_{22-43} \lesssim 0.5$ (light-blue shaded range in panel (d)), $n_{\text{cloud}} \sim (4-6) \times 10^5 \text{ cm}^{-3}$ (or an even higher one) is required. The estimated n_{cloud} is somewhat larger than the values of the dynamically estimated density (Nagai et al. 2017; Kino et al. 2018) and the density estimated by absorption lines detected by the Atacama Large Millimeter/submillimeter Array (ALMA; Nagai et al. 2019). It may indicate that the cloud has an internal structure and a denser portion may be responsible for the flattening of α_{22-43} . Another intriguing feature seen in Figure 3 is the rise of the spectral index reaching to $\alpha_{22-43} \approx 0$ in mid-2018 again. This may be caused by the FFA due to another foreground dense cloud floating around C3.

3.3. Morphological Transition of the Radio Lobe after the Collision

In Figure 4, we have shown the sequence of VLBA images of 3C 84 at 43 GHz from 2012 July to 2020 January. The emergence of this C3 was around 2003, which means that C3 is only about 15 yr old and it has been well known that the shape of C3 is similar to that of the so-called FR II-class radio lobes (Nagai et al. 2010). As shown in the top row of Figure 4, C3 continued to propagate southward by mid-2016. As in the top

row of Figure 4, during the mid-2016 to late-2017 period, the hotspot of the luminosity peak within C3 showed a frustrated trajectory of motion (see Figure 1) and a corresponding decrease in luminosity (see Figure 3). The most important finding in Figure 4 is the morphological transition of the overall structure of C3 after the breakout. A series of images taken after 2018 clearly shows that the shape of the radio lobe has distorted, losing the characteristics of FR II-class radio lobes and changing to have the characteristics of the so-called FR I-class radio lobe without a clear hotspot feature. Such a rapid change of the radio-lobe morphology has not been yet recognized. What should be emphasized here is that the jet received energy from the cloud and strongly influenced its evolution. This is opposite to the so-called radio-mode feedback where the energy is fed back from the jet to the surrounding matter (e.g., Fabian 2012).

As is also shown in Figure 4, we discovered another interesting feature, i.e., a new component moving forward in C3 (we denote it as FW). Interestingly, such behaviors are sometimes seen in numerical simulations of jet–cloud interactions (e.g., de Gouveia Dal Pino 1999; Wagner et al. 2012) and thus the FW might be understood as a circumventing portion of the propagating jet during the collision.

4. Discussions

4.1. Possible Origin of the Dense Cloud

Since matter cannot maintain a balance of forces on the axis because there is no centrifugal force acting on ambient matter, the region along the jet axis is considered to be essentially free

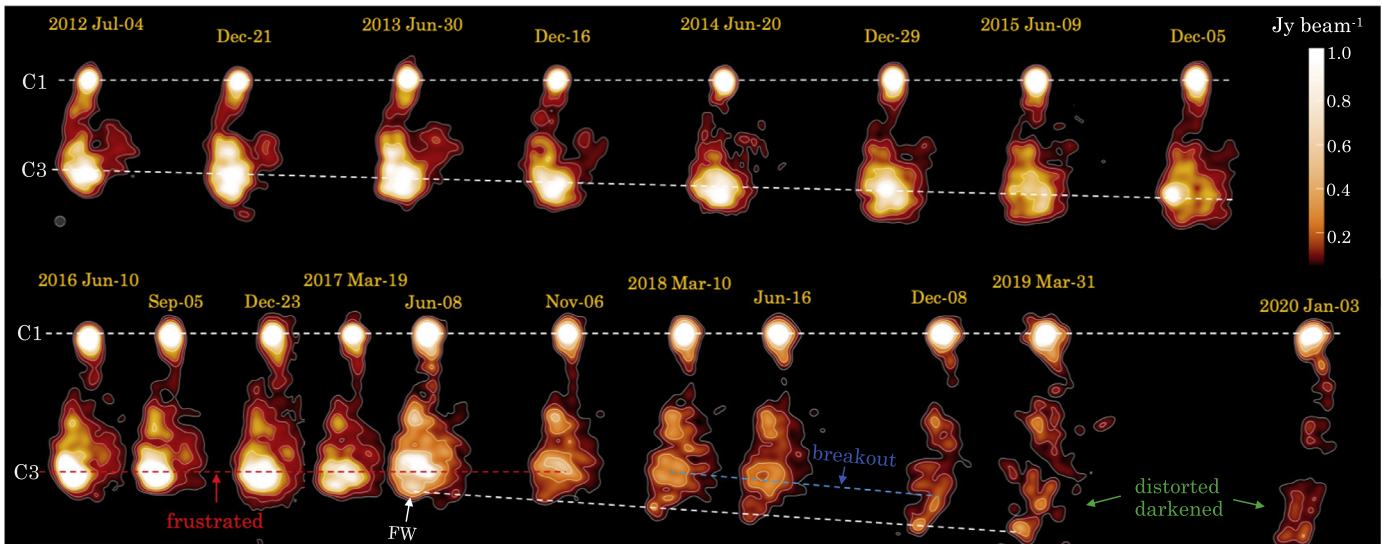


Figure 4. Sequence of the archival VLBA images of the 3C 84 jet at 43 GHz during the period from 2012 July to 2020 January (<https://www.bu.edu/blazars/>). All images are restored with a circular Gaussian beam size of 0.25 mas as shown in the bottom-left side of the first image obtained on 2012 July 4. As shown in the top row, C3 continued to propagate southward by mid-2016 (white dashed line). As in the bottom row, during the mid-2016 to late-2017 period, the hotspot of the luminosity peak within C3 showed a frustrated trajectory of motion (red dashed line). Surprisingly, appearance of the radio lobe significantly changes after the breakout. A series of images shows that the shape of the radio lobe has distorted, losing the characteristics of FR II-class radio lobes and changing to have the characteristics of the so-called FR I-class radio lobes. The new component named as FW has emerged during the frustrated phase (white dashed line in the bottom row). After 2019, the radio lobe significantly distorted and darkened.

of gas clouds (Ramos Almeida & Ricci 2017). Then, how can the cloud we have discovered exist in that region? One possible scenario might be a failed clumpy wind ejected by a different mechanism. A recent study proposes that radiation feedback drives a “fountain,” that is, a vertical circulation of clumpy gas (Wada 2012). Since this is not a centrifugal-driven wind but radiation-driven one, the driven gas fountain can occasionally come into the polar region. Another possible scenario might be a cold chaotic accretion (CCA) onto supermassive black holes (Gaspari et al. 2013). In the CCA scenario, subsequent recurrent collisions and tidal forces between clouds and filaments promote angular momentum cancellation, and it boosts accretion onto the central black hole. On subparsec scales the clouds are channeled to the center via a funnel region. Perseus cluster is an archetypal example of a cool-core cluster containing plenty of cold gas about $10^{10}M_{\odot}$ (Salomé et al. 2006) and the observed complex morphology of the CO filaments (e.g., Lim et al. 2008; Nagai et al. 2019) on kiloparsec scales seems to agree with the CCA scenario. $H\alpha$ images of the central region of NGC 1275 show features in the stellar body of NGC 1275 and identify outer stellar regions containing blue, probably young, star clusters, which can be also interpreted as recent accretion of a gas-rich system (Conselice et al. 2001), which may support CCA scenario.

4.2. New Pathway for the FR I/FR II Divide

As mentioned in the 1, two scenarios have been proposed for the origin of the FR I/FR II divide: (i) it is caused by intrinsic properties of a central engine that drives a jet, and (ii) it is caused by jet deceleration by surrounding ambient matter. Within scenario (ii), our observational finding adds a new pathway where the progenitor of a FR II radio lobe can turn into the FR I one when it strongly collides with a dense cloud on parsec scales. Although it is quite interesting to see how often such transitions occur via strong deceleration, this is the first example and little is known about it so far. Observational

studies of cold gas properties at central parsec scales of radio galaxies using ALMA would be useful in the future.

The evolution model where compact radio lobes expand and become large FR Is and FR IIs is well consistent with radio observational data (e.g., Kawakatu et al. 2008; Kunert-Bajraszewska et al. 2010; O’Dea & Saikia 2021). Kawakatu et al. (2008) studied the properties of more than 100 radio lobes and by comparing the hotspot advancing speed with the sound speed of the ambient medium, they indicated that only compact symmetric objects whose initial advance speed is faster than about $0.1c$ can evolve into FR II class. Based on the momentum balance between the jet thrust and the ram pressure by the surrounding ambient matter, Kawakatu et al. (2009) further derived a criterion value of $L_j/n_{\text{amb}} \approx 10^{44-45} \text{ erg s}^{-1} \text{ cm}^3$ that divides the evolutionary path to FR I and FR II class. Applying this criterion, we find that $n_{\text{amb}} = n_{\text{cloud}} \sim (4-6) \times 10^5 \text{ cm}^{-3}$ can easily make the jet frustrated. The obtained n_{cloud} is roughly comparable to the one that caused the jet flip (Kino et al. 2018), so what could have caused such a difference? It could be interpreted that the flip event was an off-axis collision with a small single cloud, while the frustration event was a head-on collision with a sort of multiple cloud assembly.¹⁴

Since the cloud is of finite size, the jet breaks out of the cloud in a finite time. After the jet breakout, the deposited E_{feedback} would be spent for energy-driven expansion of the radio lobes. By approximating the expansion as an E_{feedback} -driven Sedov–Taylor one (e.g., Ostriker & McKee 1988), the predicted expansion velocity can be estimated as $v_{\text{exp}} \approx 0.2c \left(\frac{E_{\text{feedback}}}{10^{51} \text{ erg}} \right)^{1/5} \left(\frac{n_{\text{cloud}}}{10^5 \text{ cm}^{-3}} \right)^{-1/5} \left(\frac{t}{1 \text{ yr}} \right)^{-3/5}$, which shows a reasonable agreement with the C3 advancing speed seen in

¹⁴ On the other hand, when a jet thrust is stronger than the ram pressure from surrounding clouds, radio-mode feedback would be in action as was indicated in a young radio jet source 4C 12.50 (e.g., Morganti et al. 2013).

Figure 4.¹⁵ Further VLBI monitoring observations of 3C 84 in the future will update this rough-cut order estimation of v_{exp} .






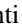



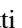

What would it be expected if such a strong a jet–cloud collision generally happens and influences of FR I/II divide? Then, the FR I/II divide would reflect information on the dense gas along the jet axis. For instance, the archetypal FR II class Cygnus A may be free from strong collisions with cold dense gas at its central region, since Cygnus A has classical double radio lobes. The central cooling time of the Cygnus A cluster is about 10 times longer than the Perseus cluster (Fabian 1994) and the longer cooling time may realize a CCA-free environment. On the other hand, the Perseus cluster indeed contains filamentary cold molecular gas at its center (e.g., Salomé et al. 2006; Lim et al. 2008). It is also known that there are multiple radio bubbles in various directions (Pedlar et al. 1990). One may guess that such radio bubbles could be remnants whose progenitors are young bubbles that underwent strong CCA–jet collisions. We further point out the case of 4C 31.04, a source with an FR II morphology on parsec scales and a luminosity that is predicted to evolve in an FR I large-size object (Giroletti et al. 2003): similarly to 3C 84, the hotspots of 4C 31.04 are known to produce feedback on the surrounding gas (Zovaro et al. 2019). However, differently from 3C 84, there is no direct evidence for any morphological transition in that source, perhaps due to the lack of high-cadence observations or perhaps because of a different mechanism not involving jet–CCA interactions.

Asymmetries in young radio lobes also suggest interactions between radio jets and environment (Saikia & Gupta 2003). Interestingly, it is found that a fairly large fraction ($\sim 50\%$) of asymmetric compact radio lobes have brighter lobes closer to the nucleus that can be understood as jet–cloud interactions (Dallacasa et al. 2013; Orienti 2016). It is curious that a hotspot can be both brightened and diminished by a collision. It may imply that behavior of the radio flux densities of those hotspots highly depends on positional relationships between the jet and clouds. In some cases, clouds may cover up the hotspot like the present case of 3C 84, while in other cases, they may be exposed without being obscured (Dallacasa et al. 2013; Orienti 2016). Aside from the need for further research on the curious behavior of radio flux densities, the existence of young asymmetric radio lobes also suggests that jet–cloud interaction on parsec scales is ubiquitous.

This work is mainly based on KaVA observations, which is operated by the Korea Astronomy and Space Science Institute (KASI) and the National Astronomical Observatory of Japan (NAOJ). This work is partially supported by JSPS/MEXT KAKENHI (grants JP18K03656, JP18H03721, JP18K03709, JP21H01137, 19K03918) and by Korea’s National Research Council of Science and Technology (NST) granted by the International joint research project (EU-16-001). We thank A. Hirano for her cooperation of VERA 22 GHz data analysis. This study makes use of 43 GHz VLBA data from the VLBA-BU Blazar Monitoring Program (VLBA-BU-BLAZAR; <http://www.bu.edu/blazars/>), funded by NASA through the Fermi Guest Investigator Program. VLBA is an instrument of the Long Baseline Observatory. The Long Baseline Observatory is a facility of the National Science Foundation operated by

Associated Universities, Inc. The Submillimeter Array is a joint project between the Smithsonian Astrophysical Observatory and the Academia Sinica Institute of Astronomy and Astrophysics and is funded by the Smithsonian Institution and the Academia Sinica.

ORCID iDs

Motoki Kino  <https://orcid.org/0000-0002-2709-7338>
 Kotaro Niinuma  <https://orcid.org/0000-0002-8169-3579>
 Nozomu Kawakatu  <https://orcid.org/0000-0003-2535-5513>
 Hiroshi Nagai  <https://orcid.org/0000-0003-0292-3645>
 Gabriele Giovannini  <https://orcid.org/0000-0003-4916-6362>
 Monica Orienti  <https://orcid.org/0000-0003-4470-7094>
 Kiyooki Wajima  <https://orcid.org/0000-0003-3823-7954>
 Filippo D’Ammando  <https://orcid.org/0000-0001-7618-7527>
 Kazuhiro Hada  <https://orcid.org/0000-0001-6906-772X>
 Marcello Giroletti  <https://orcid.org/0000-0002-8657-8852>
 Mark Gurwell  <https://orcid.org/0000-0003-0685-3621>

References

- Baum, S. A., Zirbel, E. L., & O’Dea, C. P. 1995, *ApJ*, 451, 88
 Churazov, E., Forman, W., Jones, C., & Böhringer, H. 2000, *A&A*, 356, 788
 Conselice, C. J., Gallagher, J. S. I., & Wyse, R. F. G. 2001, *AJ*, 122, 2281
 Croton, D. J., Springel, V., White, S. D. M., et al. 2006, *MNRAS*, 365, 11
 Dallacasa, D., Orienti, M., Fanti, C., Fanti, R., & Stanghellini, C. 2013, *MNRAS*, 433, 147
 de Gouveia Dal Pino, E. M. 1999, *ApJ*, 526, 862
 Fabian, A. C. 1994, *ARA&A*, 32, 277
 Fabian, A. C. 2012, *ARA&A*, 50, 455
 Fanaroff, B. L., & Riley, J. M. 1974, *MNRAS*, 167, 31P
 Fujita, Y., & Nagai, H. 2017, *MNRAS*, 465, L94
 Gaspari, M., Ruszkowski, M., & Oh, S. P. 2013, *MNRAS*, 432, 3401
 Ghisellini, G., & Celotti, A. 2001, *A&A*, 379, L1
 Giovannini, G., Savolainen, T., Orienti, M., et al. 2018, *NatAs*, 2, 472
 Giroletti, M., Giovannini, G., Taylor, G. B., et al. 2003, *A&A*, 399, 889
 Gurwell, M. A., Peck, A. B., Hostler, S. R., Darrah, M. R., & Katz, C. A. 2007, in ASP Conf. Ser. 375, From Z-Machines to ALMA: (Sub)Millimeter Spectroscopy of Galaxies, ed. A. J. Baker et al. (San Francisco, CA: ASP), 234
 Heinz, S., Reynolds, C. S., & Begelman, M. C. 1998, *ApJ*, 501, 126
 Hiura, K., Nagai, H., Kino, M., et al. 2018, *PASJ*, 70, 83
 Kawakatu, N., Kino, M., & Nagai, H. 2009, *ApJL*, 697, L173
 Kawakatu, N., Nagai, H., & Kino, M. 2008, *ApJ*, 687, 141
 Kharb, P., O’Dea, C. P., Tilak, A., et al. 2012, *ApJ*, 754, 1
 Kino, M., Wajima, K., Kawakatu, N., et al. 2018, *ApJ*, 864, 118
 Komatsu, E., Dunkley, J., Nolta, M. R., et al. 2009, *ApJS*, 180, 330
 Kormendy, J., & Ho, L. C. 2013, *ARA&A*, 51, 511
 Kunert-Bajraszewska, M., Gawroński, M. P., Labiano, A., & Siemiginowska, A. 2010, *MNRAS*, 408, 2261
 Läing, R. A., & Bridle, A. H. 2014, *MNRAS*, 437, 3405
 Levinson, A., Laor, A., & Vermeulen, R. C. 1995, *ApJ*, 448, 589
 Lim, J., Ao, Y., & Dinh-V-Trung 2008, *ApJ*, 672, 252
 Meier, D. L., Edgington, S., Godon, P., Payne, D. G., & Lind, K. R. 1997, *Natur*, 388, 350
 Morganti, R., Fogasy, J., Paragi, Z., Oosterloo, T., & Orienti, M. 2013, *Sci*, 341, 1082
 Nagai, H., Fujita, Y., Nakamura, M., et al. 2017, *ApJ*, 849, 52
 Nagai, H., Kino, M., Niinuma, K., et al. 2013, *PASJ*, 65, 24
 Nagai, H., Onishi, K., Kawakatu, N., et al. 2019, *ApJ*, 883, 193
 Nagai, H., Suzuki, K., Asada, K., et al. 2010, *PASJ*, 62, L11
 Niinuma, K., Lee, S.-S., Kino, M., et al. 2014, *PASJ*, 66, 103
 O’Dea, C. P., & Saikia, D. J. 2021, *A&AR*, 29, 3
 Orienti, M. 2016, *AN*, 337, 9
 Ostriker, J. P., & McKee, C. F. 1988, *RvMP*, 60, 1
 Pedlar, A., Ghataure, H. S., Davies, R. D., et al. 1990, *MNRAS*, 246, 477
 Ramos Almeida, C., & Ricci, C. 2017, *NatAs*, 1, 679
 Rawlings, S., & Saunders, R. 1991, *Natur*, 349, 138

¹⁵ The advancing speed of C3 with 5 mas averaged over 17 yr corresponds to the apparent speed as $\beta_{\text{app}} \sim 0.33$. Together with the jet viewing angle $18^\circ \lesssim \theta_{\text{view}} \lesssim 40^\circ$, a relatively fast speed of $0.35 \lesssim \beta \lesssim 0.53$ is estimated.

- Saikia, D. J., & Gupta, N. 2003, *A&A*, 405, 499
- Salomé, P., Combes, F., Edge, A. C., et al. 2006, *A&A*, 454, 437
- Scharwächter, J., McGregor, P. J., Dopita, M. A., & Beck, T. L. 2013, *MNRAS*, 429, 2315
- Scheuer, P. A. G. 1982, in IAU Symposium, Extragalactic Radio Sources, 97, ed. D. S. Heeschen & C. M. Wade (Cambridge: Cambridge Univ. Press), 163
- Suzuki, K., Nagai, H., Kino, M., et al. 2012, *ApJ*, 746, 140
- Wada, K. 2012, *ApJ*, 758, 66
- Wagner, A. Y., Bicknell, G. V., & Umemura, M. 2012, *ApJ*, 757, 136
- Wajima, K., Kino, M., & Kawakatu, N. 2020, *ApJ*, 895, 35
- Walker, R. C., Dhawan, V., Romney, J. D., Kellermann, K. I., & Vermeulen, R. C. 2000, *ApJ*, 530, 233
- Zovaro, H. R. M., Sharp, R., Nesvadba, N. P. H., et al. 2019, *MNRAS*, 484, 3393